Detection of Signal and Ground Photons From ICESat-2 ATL03 Data

Xiangxi Tian and Jie Shan, *Senior Member, IEEE*

***Abstract*— The Advanced Topographic Laser Altimeter System (ATLAS) laser altimeter aboard the Ice, Cloud, and Land Elevation Satellite (ICESat-2) can measure the elevation of the Earth's surface with unprecedented spatial detail. However, the quality of the derived signal and ground photons depends on the signal-to-noise ratio and canopy coverage. Current algorithms underperform for data collected during daytime over mountain areas with dense canopy. We demonstrate a novel procedure for signal photon detection and subsequent ground photon detection from ICESat-2 ATL03 data. We first introduce a gravity-based density model to characterize the anisotropic properties of photon distribution. Through jointly using the photon densities from the weak–strong beam pair, we are able to find key photons that have high probability being signals. A directional regional growing approach then takes these key photons as seeds to label all remaining signal photons. Finally, we introduce a weighted iterative median filter (WIMF) algorithm to identify ground photons whose height is closest to the estimated ground surface. A total of 36 ATL03 beams of two entire counties in USA are used for test and evaluation. Compared to the ATL03 and ATL08 algorithms, our signal photon finding method is more robust to the variation of topography, canopy coverage, and data collection time. Remarkably, the mislabeling caused by the after-pulsing effect does not present in our detected signal photons. Comparing current ATL03 and ATL08 products, the detected ground photons from our method are more consistent with reference to the 3DEP DEM, especially for strong beam data collected during daytime in dense canopy, high relief areas.**

***Index Terms*— Advanced Topographic Laser Altimeter System (ATLAS), after-pulsing effect, ATL03, ATL08, gravity-based density, Ice, Cloud, and Land Elevation Satellite (ICESat-2), photon counting lidar.**

I. Introduction

SPACEBORNE lidar is an advanced technology to directly acquire the vertical dimension and thus to derive many height-related information for global scientific studies. Launched in 2003, Geoscience Laser Altimeter System (GLAS) onboard the Ice, Cloud, and Land Elevation Satellite (ICESat) provided worldwide lidar waveform data until October 2009 [1]. The primary purpose of ICESat was to determine interannual and long-term changes in polar ice-sheet volume (and inferred mass change) with sufficient accuracy to assess their impact on global sea level [2]. As a follow-on of the ICESat mission, NASA launched ICESat-2 on September 15, 2018, primarily to measure changes in land ice elevation and sea-ice freeboard and to enable the determination of vegetation canopy height globally [3], [4]. The instrument for height determination on the ICESat-2 observatory is the Advanced Topographic Laser Altimeter System (ATLAS). The design of ATLAS is based on the success and limitations of the GLAS aboard ICESat [3]. In ATLAS, a 532-nm laser light at a pulse repetition frequency of 10 kHz is split into six beams. These six beams are arranged into three pairs of weak beam and strong beam [4]. This configuration allows the measurement of the surface slope in both the along- and across-track directions with a single pass and the measurement of height change from any two passes over the same site [4].

ICESat-2 provides several data products to the science community and the general public [4]. Among the products of ICESat-2, the Level 1B data product, denoted as ATL02, provides the ATLAS time of flight, ATLAS housekeeping data, and other data necessary for science data processing. The Level 2A data product, identified as ATL03, provides the latitude, longitude, and ellipsoidal height of photons detected by the ATLAS instrument. Based on the ATL03 data product, higher level (Level 3A) surface-specific data products consist of glacier and ice sheet height, sea ice freeboard, vegetation canopy height, ocean surface topography, and inland water body height [4].

The most distinct characteristic of the ATLAS data is that a large number of noise photons may present both above and below the ground surface. Noise photons above the ground surface are due to the backscatter effect arising from clouds and aerosols [5] as well as solar background noise [6], [7]. Due to the high sensitivity of the photomultiplier tube (PMT) detector in ICESat-2, the detectors can respond to a single photon. Even though narrow bandpass filtering is implemented aboard ATLAS to constrain the received light to 532 nm, a significant amount of sunlight of the same wavelength will be simultaneously recorded [8]. As a result, the measured geolocated photons are usually very noisy, especially during the daytime when solar radiance is strong [9]. For noise photons below the ground surface, they are introduced by the after-pulsing effect of the detector [5]. After-pulses are presented in ATLAS data regardless of surface reflectance; however, they can be most easily characterized as the strong signal returns measured from high reflectance surfaces above which there is minimal atmospheric attenuation. After-pulsing effect of ATLAS is usually triggered by three distinct sources: ionization effects within the PMTs, internal optical reflections in the receiver, and detector saturation and dead-time recovery [10]. The ionization effects within the PMTs are usually

Manuscript received 25 July 2022; revised 31 October 2022; accepted 18 December 2022. Date of publication 27 December 2022; date of current version 6 January 2023. *(Corresponding author: Jie Shan.)*

The authors are with the School of Civil Engineering, Purdue University, West Lafayette, IN 47907 USA (e-mail: tian133@purdue.edu; jshan@purdue.edu).

Digital Object Identifier 10.1109/TGRS.2022.3232053

accounted for time delay with respect to the primary signal output pulse range from several hundred nanoseconds to over a few microseconds (or equivalently several tens of meters to hundred meters). The time delay caused by internal optical reflection is the multiple of the effective optical path length (EOPL) from the telescope to the detector. The dead-time recovery is the major source of the after-pulse appearing from ∼0.45 to ∼1.8 m after the first return peak, which is determined by ATLAS's dead time of ∼3 ns [11], corresponding to a distance of ∼0.45 m between the primary and secondary echoes.

Since the working principles of ATLAS are quite different from conventional spaceborne lidar and the terrain characteristics vary significantly in terms of land cover, many specific signal finding algorithms have been proposed by several research teams. Magruder et al. [9] proposed three methods to discard noise photons from the Multiple Beam Experimental LiDAR (MABEL), which is an experimental airborne mock-up for ATLAS. The noise filtering method for producing the ATL03 product is a histogram-based algorithm proposed by Neumann et al. [12]. It first constructs histograms with photons aggregated into along-track and vertical bins. Signal photons are then distinguished from noise photons by a series of threshold based tests. As a result, each photon is assigned with a confidence level indicating how likely it is signal or noise. Neuenschwander and Pitts [13] proposed an inspiring and effective algorithm to detect signal photons and ground photons. The complete procedure consists of two steps, signal photon finding by the differential, regressive, and Gaussian adaptive nearest neighbor (DRAGANN) algorithm and ground photon finding by a median filter (MF)-based smoothing filtering algorithm [13]. The procedure has been proven to have a good performance on ICESat-2 ATLAS data in land-vegetation areas [13] and has been used to process ATL03 data and generate the mission's ATL08 products [14].

Beside the above two methods used for ATLAS by NASA, there are many additional efforts made by researchers. Zhang and Kerekes [15] applied the density-based spatial clustering of applications with noise (DBSCAN) algorithm to detect signal photons from geolocated photons measured by photon-counting laser altimeters. Based on the work of Zhang and Kerekes, Ma et al. [5] proposed an adaptive thresholding strategy in the DBSCAN algorithm to find the signal photons for MABEL datasets. Nie et al. [16] further modified the DBSCAN algorithm by rotating the elliptical searching neighborhood in all directions, which can be applied to extract tree canopy as well as terrain profile for MABEL datasets. Zhu et al. [17] applied Nie's algorithm to ICESat-2 and retrieved the vegetation height. In these studies, the volume and direction of the ellipsoid searching area were determined by a principal component analysis (PCA) method. However, the study areas of all above research were relatively flat with an elevation change less than 20 m. Zhang et al. [18] demonstrated the relation between the signal-to-noise ratio (SNR) and several influential factors, including beam type, data collection time, and topography. As the slope increases, the SNR decreases sharply, and the same pattern applies for the sun presence and the SNR as well [18]. Such situations become worse for the weak beam due to a further decrease on the SNR caused by a lower transmit energy [18]. Therefore, Zhang et al. [18] took the advantage of the relationship between SNR and slope obtained from the strong beam to estimate the along-track slope of the corresponding weak beam and succeeded in identifying more reliable signal photons for the weak beam in mountain areas. However, their research area did not contain much forest coverage.

The shortfalls of current work are threefold. First, among all the existing signal finding and ground finding algorithms for ATLAS, they mostly treat the strong beam and weak beam separately. That means the algorithms only consider the terrain information in the along-track direction, one by one independently. The advantages provided by and the information embedded in the strong–weak beam pairs in the ATLAS configuration are ignored. As a result, these methods are likely vulnerable for complex terrain with medium or high relief and heavy canopy. Second, dense canopy coverage would introduce more difficulties to ground detection in mountain areas. Although this may not affect the SNR for signal photon detection, there is little effort on dealing with such areas for ground detection. Third, current density-based research on ICESat-2 uses a conventional method (such as DBSCAN) to calculate the density by counting the number of points within a certain region, sphere, or ellipsoid. However, this is not sufficient and realistic when the distribution of photons is heterogeneous and anisotropic.

Inspired by previous research, the motivation of this study is to improve the signal finding and ground finding results for current ATL03 product. It includes two aspects: eliminating the noise photons to detect signal photons and then identifying only ground photons from the signal photons. For signal photon detection, the major challenge is to handle the unusually high rate of noises in the recorded data, whereas the difficulty for ground photon detection is to find the true ground under the interruption of dense canopy photons. This research aims to detect signal photons from very low SNR data (caused by the low laser energy, sun presence, and large terrain slope) and then extract reliable ground photons from the detected signal photons, especially for areas covered by dense canopy.

The rest of this article is structured as follows. Section II describes the methodology in detail along with illustrative examples. Section III introduces the areas of interest and the data used in this study. In Sections IV and V, the representative results on signal detection and ground detection are, respectively, presented and discussed. At last, conclusion is described in Section VI.

II. Methods

To find the signal photons and ground photons, it is vital to understand their properties first. Therefore, two essential observations are made to identify the characteristics of photons from different types of targets. As shown in Fig. 1, the first observation is that the signal photons are clustered together, i.e., have higher density than noise, which is sparsely and randomly distributed in all directions. The second observation is related to ground photons and canopy photons, both of which are regarded as signals. As a subset of signal photons, ground photons, though clustered in space, have higher density

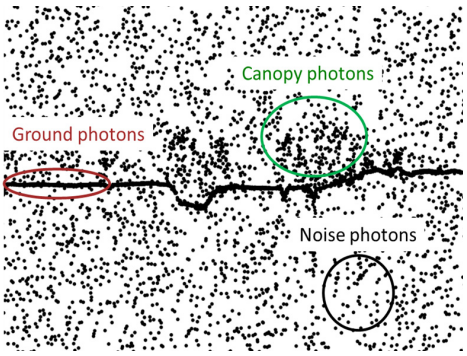

Fig. 1. Anisotropic density characteristics of noise, ground, and canopy photons.

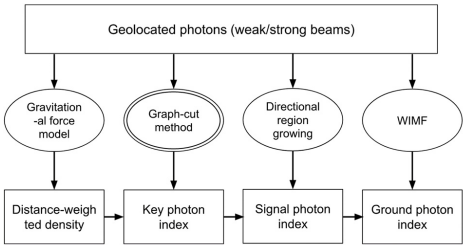

Fig. 2. Flowchart of signal and ground photon detection with the developed GRADWIT method. The double circle indicates that the density information of both weak and strong beams are jointly used.

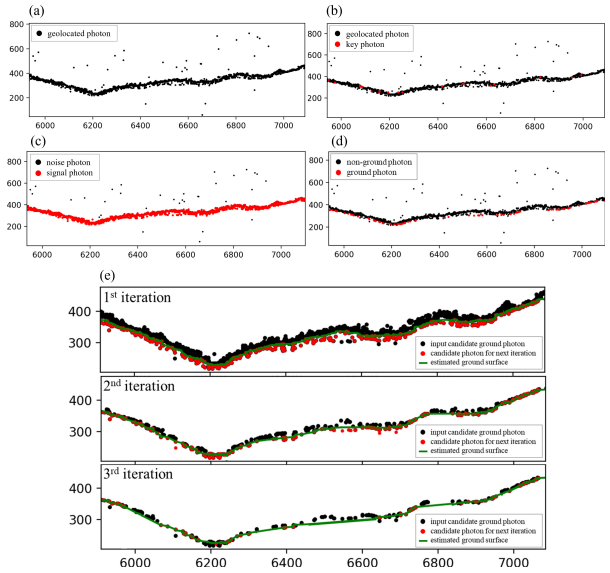

Fig. 3. Examples of the proposed workflow for signal and ground photon detection. The data are from a strong beam. The horizontal axis represents the distance along the track in meters, and the vertical axis is the ellipsoid height in meters. (a) Raw data as input. (b) Key photon finding results. (c) Signal photon finding results. (d) Ground photon finding results. (e) Procedure of WIMF for ground surface estimation.

in the horizontal direction than in the vertical direction. The canopy photons, as another subset of signal photons, have the opposite property, i.e., their vertical density is higher than the one in the horizontal direction. Such different, anisotropic density properties will be used to remove noise and detect signal photons from the recorded photons and further to differentiate ground photons with canopy photons.

The flowchart of the entire process is illustrated in Fig. 2, and the corresponding results from each step are shown in Fig. 3. To detect signal photons and ground photons, the input data are the geolocated photons of the weak–strong beam pairs, i.e., the ATL03 product. The process consists of four sequential steps: gravitational force model for photon density definition, graph-cut optimization for selection of key signal photons, directional regional growing for signal detection, and weighted iterative MF for ground detection, or for short, GRADWIT. It starts with photon density calculation for photons in each beam separately. Photons that have high probability being signals, i.e., key photons, are found for the strong and weak beams, where density information of both weak and strong beams are jointly utilized. The key photons are then regarded as seeds, followed by a directional regional growing to label all possible remaining signal photons. Based on the labeling output of the signal photon algorithm and the density direction calculated in the first step, a weighted iterative median filter (WIMF) algorithm is conducted to find the estimated ground surface. Photons whose height is close to the estimated ground surface are labeled as ground photons. The following section will discuss: 1) gravity-based density; 2) key photon selection; 3) signal photon finding; and 4) ground photon finding.

A. Gravity-Based Photon Density Model

Density is an essential metric for several lidar filtering methods. The DBSCAN [19] method and its variants are among the most commonly used ones. The typical method to calculate density in DBSCAN is by counting the number of points within a certain region, sphere, or ellipsoid [16]. Despite the fact that it considers the density distribution in the entire dataset by sorting the points [16], one of the deficiencies is that the distribution or specific clustering patterns within a certain region cannot be well reflected by the number of points. Conventional density calculation method only considers the count of photons and their distances. However, we argue that this is not sufficient and may lead to vulnerability, since density can be anisotropic as we pointed out above. Therefore, we intend to introduce a gravitational method to calculate the density more realistically, which has physical insight to the clustering of photons with their neighbor photons. The idea of using gravitational model has been adopted in clustering. In 1977, inspired by the gravitational attraction in physics, Wright [20] proposed the gravitational clustering algorithm for performing the clustering analysis. In recent years, several researchers further explored the potential of the gravitational clustering method, by regarding each data point as an object with mass and associating a data gravitational force with each data point generated by its neighbors [21]. Based on the data gravitational force, the position of each data point would be updated at each iteration and aggregated into clusters [22]. The use of data gravitational force (including its magnitude and direction) in clustering can be regarded as a variant of density-based clustering method [22]. To some extent, the data gravitational force can be considered as a similarity measure, which takes both distance and direction among data points into account [21]. On top of that, we introduce the gravity-based density concept or simply referred as density in the

following discussion unless otherwise specified. We then use this density model to describe the clustering properties of geolocated photons in ATLAS data.

The gravitational attraction force on a photon is the sum of all forces applied by its neighboring photons [23]

$$\boldsymbol{F}_i = \Sigma_{j \in N_i} G \frac{m_i m_j}{\|\boldsymbol{r}_{ij}\|^2} \boldsymbol{r}_{ij} \tag{1}$$

where N_i denotes all neighboring photons around the target photon, $\boldsymbol{F}_i$ is the total gravitational force applied to photon i, j stands for its neighboring photon, G is the gravitational constant, m_i and m_j are the masses of photons i and j, and $\boldsymbol{r}_{ij}$ is the vector between the two photons. In our case, it is convenient to make the mass of a photon equal to 1 and the gravitational constant G be 1. The total gravitational force on a photon is related to the number of the neighboring photons and the distance and direction to its neighboring photons. By examining the total gravitational forces on a photon, not only the number of the neighboring photons can be evaluated but also the distribution of the neighboring photons. Therefore, the gravity-based density $\boldsymbol{\rho}_i$ of a photon p_i, as a vector, is defined by the sum of the magnitude of the gravitational force from its neighbor photons

$$\boldsymbol{\rho}_i = \left(\sum_{j \in N_i} \frac{1}{\|\boldsymbol{r}_{ij}\|^2} \right) \boldsymbol{v}_i \tag{2}$$

and its direction $\boldsymbol{v}_i$ is defined by

$$\boldsymbol{v}_i = \sum_{j \in N_i} \frac{\boldsymbol{r}_{ij}}{||\boldsymbol{r}_{ij}||}. \tag{3}$$

For the convenience of expression, the magnitude of the density $||\boldsymbol{\rho}||$ is denoted as ρ in the following discussion. As a vector, the magnitude of our density is used to reflect the aggregation of a photon, and the direction of the density can reflect its anisotropic properties, i.e., the varying clustering patterns of the neighboring photons in different directions around the target photon. Since the impact of a photon on another photon would greatly increase as the distance between them decreases, a photon can have a very different density even if the number of neighboring photons remains unchanged. Moreover, the direction of the density mirrors the anisotropic distribution of the neighboring photons, which is essential for the following anisotropic filtering to separate canopy photons and ground photons.

To separate ground photons and canopy photons, recall the second observation made in the beginning, the density of ground photons is anisotropic in different directions. Such anisotropy shall be reflected by the calculated density direction. The density direction of ground photons without canopy on top would be mostly along the horizontal direction, whereas for ground photons beneath the canopy and canopy photons themselves, their density direction is along the vertical direction. To consider this observation, a local coordinate system is set on each signal photon, in which the x-axis refers to the slope direction of the ground surface and the y-axis denotes the direction perpendicular to the ground surface, i.e., the direction of vegetation growth. Under this local coordinate system, an angle of the density direction, in radians from $-\pi$ to π, with respect to the x-axis can be calculated. We use the following three distinct scenarios to illustrate this concept. For the first scenario, as shown in Fig. 4, for a ground photon without canopy presence, its density direction would lean to the x-axis (ground surface direction) and the angle of the density direction is close to 0, whereas for a ground photon beneath canopy, its density direction would be more parallel to the y-axis and the angle is positive. For a canopy photon, the angle of its density direction is negative. Based on this evaluation, an index ω_i is proposed to describe the probability of a signal photon p_i being a ground photon

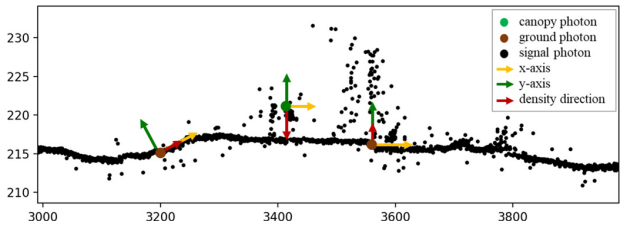

Fig. 4. Directional distribution of density for canopy photon (green dot) and ground photon (brown dots) with respect to all detected signal photons (black dots). The horizontal axis represents the distance along the track in meters, while the vertical axis is the ellipsoid height in meters.

$$\omega_i = \begin{cases} \exp(\theta_i), & \theta_i < 0 \\ 1, & \theta_i \geq 0 \end{cases} \tag{4}$$

in which $\theta_i = \arccos(\boldsymbol{v}_i \cdot \boldsymbol{u}_i)$ denotes the angle of density direction $\boldsymbol{v}_i$ with respect to the x-axis. The x-axis is defined by the first principal component $\boldsymbol{u}_i$ in the PCA [24] at p_i and its neighboring signal photons.

From the definition of the anisotropic index, its value is related to the angle between the density direction and direction of ground surface (slope). For a ground photon without canopy photons on top (the brown dot to the left of Fig. 4), the detected signal photons above and below the ground surface would be almost even. Thus, its density direction would be parallel to the direction of the ground surface, resulting in the anisotropic index lean to 1, which means that the probability of the photon being a ground photon is close to 1.

For a ground photon beneath the canopy (the brown dot to the right of Fig. 4), there are more detected signal photons above the ground surface than below the ground. Its anisotropic index equals to 1 due to a positive angle of density direction θ, which implies that its probability being a ground photon is 1, while for the canopy photon (the green dot in Fig. 4), due to the unevenly distributed signal photons, θ is negative; its anisotropic index is less than 1, yielding a small probability being a ground photon. In this way, by calculating the anisotropic index for each signal photon, the probability of a signal photon being a ground photon is predefined as the weight feature for the following filtering operation.

B. Selection of Key Photons

We define the key photons as a set of photons that have the greatest probability being signal photons. In particular, we state that key photons not only themselves have relatively

large density, their neighboring photons from the other beam of the weak–strong beam pair should also have high density. To select key photons, we mostly utilize the magnitude of the density or density for short. For a track of one beam (either weak or strong), we will simultaneously consider the photon density in the other beam of the weak–strong beam pair. To be specific, a set of key photons $P_K = \{k_1, k_2, \ldots, k_n\}$ are defined as

$$\text{argmin}_{\boldsymbol{P}_K}\left(\sum_{i=1}^{n}\frac{1}{\rho_i \times \hat{\rho}_i}\right) \tag{5}$$

where ρ_i refers to the magnitude of density of an interest photon i and $\hat{\rho}_i$ is the density of its nearest (in terms of distance) neighbor photon in the other beam of the weak–strong beam pair.

One of the major characteristics of ATLAS is that each pair of beams consists of a strong beam and a weak beam in the cross-track direction, whose ground distance is ~90 m and whose laser energy ratio is 4:1. In consequence, there would be much fewer received photons from the weak beam than from the strong beam. The signal photons are much harder to identify for weak beams than for strong beams. However, the land cover or topography is not likely to vary much within a neighborhood of 90 m, and (5) essentially means the key photons are those that have local maximum densities considering both along- and across-track directions. As shown in Fig. 3(b), such determined key photons are expected to be reliable signal photons.

After calculating the density for each photon, the signal photon finding problem can be treated as a labeling problem, i.e., every photon in a dataset will be labeled as either signal or noise. The problem is to find the key photons $P_K = \{k_1, k_2, \ldots, k_n\}$ with the objective function as (5). To this end, we use the graph-cut method [25], [26]. Adapted from the application of Ural and Shan [27], we first build a graph $G = \{V, E; t_G\}$, which consists of a set of vertices or nodes V, a set of edges E between nodes, and an incidence relation t_G, which maps the pairs of elements of V to elements of E. The set of nodes V is composed of all unassigned photons from the target beam and two special nodes, source (s), and sink (t). Each recorded photon is a node in the graph, and it is connected to its 3-D Voronoi neighbors with the edges of the graph. Moreover, all unassigned photons are connected to the source and sink, which represent the labels (signal and noise). The energy function for the labeling problem is defined as [27]

$$E(p) = E_{\text{data}}(p) + E_{\text{smooth}}(p). \tag{6}$$

The first term in the energy function (6) is the data cost, which is the cost for assigning signal or noise labels to each photon. The second term is the smoothness cost, which represents the weights of the edges connecting photons with their Voronoi neighbors. In this research, the data cost term is defined by

$$E_{\text{data}}(p) = \sum_{i}\frac{1}{\rho_i \times \hat{\rho}_i} \tag{7}$$

in which ρ_i is the magnitude of the density of photon p_i, and $\hat{\rho}_i$ is the magnitude of the density of the nearest photon in the other beam of the weak–strong beam pair.

The smoothness cost is calculated by the similarity between the density of the target photon and its Voronoi neighbors

$$E_{\text{smooth}}(p) = \sum_{i,j}\exp\left\{\left|\boldsymbol{\rho}_i \cdot \boldsymbol{\rho}_j(i)\right|\right\} \tag{8}$$

where $\boldsymbol{\rho}_j(i)$ is the gravity-based density of the jth Voronoi neighbor of photon p_i. The smoothness cost is a way to quantify the similarity between a photon and its neighbor. A small difference between the magnitudes of their density will enlarge the similarity between the photons and cause a large smoothness cost.

C. Detection of Signal Photons

Once the key photons are identified, they will gauge the process to extract all other signal photons. To this end, we introduce a directional region growing approach. Unlike the conventional region growing method [28], [29] that uses one fixed distance threshold Δd to define one circular search region around the seeds (key photons), the distance threshold Δd of directional regional growing is a set of adaptive distances, which defines at least one rotated elliptical search region at each seed [30]. The density threshold $\Delta\rho$ is also adaptive for each key photon. For an unassigned photon (x, y, ρ), if it meets the following conditions, it will be labeled as a signal photon

$$\begin{cases} e(j)\cdot\sqrt{(x-\bar{x}_i(j))^2 + \dfrac{(y-\bar{y}_i(j))^2}{e^2(j)-1}} \le \Delta d_i(j) \\ \rho_i \ge \Delta\rho_i(j) \end{cases} \tag{9}$$

in which $[\bar{x}_i(j), \bar{y}_i(j)]$ is the centroid of the jth search region, $e(j)$ is the eccentricity of the elliptical search region, and $\Delta\rho_i(j)$ is the threshold of the jth search region.

For a key photon p_i and its two next adjacent key photons p_{i+1} and p_{i+2}, the number of the search regions m equals to one if the angle α_i between $\overrightarrow{p_i p_{i+1}}$ and $\overrightarrow{p_{i+1} p_{i+2}}$ is smaller than a threshold $\Delta\alpha$; otherwise, it is set to two. The logic for setting multiple search regions around each key photon is that, if $\alpha_i \ge \Delta\alpha$, the key photon p_{i+1} is very likely to be a signal photon from canopy top; meanwhile, p_{i+2} is very likely to be a signal photon from ground. We want to include all potential signal photons right beneath the canopy top; otherwise, they would be easily missed.

Fig. 5 illustrates the directional regional growing process. The top panel shows the region growing procedure at the ith key photon (green dot). Since the angle $\alpha_i < \Delta\alpha$, it has one search region and is demonstrated as the light blue circle. The bottom panel shows the region growing procedure at the $(i+1)$th key photon (green dot). After the growing procedure at the ith key photon, several unassigned photons have been assigned as signal photons (orange dots) compared to the top panel. For the $(i+1)$th key photon, it has two search regions (light blue circles) since the angle $\alpha_{i+1} \ge \Delta\alpha$. Photons within the two search regions will be labeled as signal photons if they meet the density threshold.

In summary, the directional region growing algorithm works on every key photon p_i in the key photon set P_K sequentially with all unassigned photons as the demonstration shown in

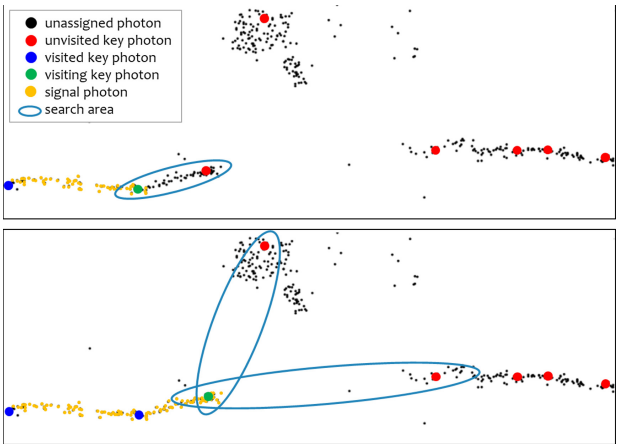

Fig. 5. Demonstration of directional region growing at two sequential photons (top: ith key photon; bottom: $(i+1)$th key photon).

Fig. 5. At the end of the directional region growing, all signal photons are identified, as shown in Fig. 3(c).

D. Detection of Ground Photons

The input to this procedure is the signal photons $S = \{s_1, \ldots, s_m\}$ detected from the previous step. The detection of ground photons in the presence of canopy poses a significant challenge due to the fact that there are often fewer ground photons underneath the canopy [3]. The key to this task is to find a continuous ground surface, for which we introduce a WIMF.

Let $G = \{g_1, \ldots, g_m\}$ be the discrete best estimation of the ground surface we could achieve from the signal photons S, then the set of signal photons can be considered as $S = G + E$, in which $\mathrm{E} = \{e_1, \ldots, e_m\}$ denotes the residuals for signal photons. The residuals E can be regarded as the nonground height bias introduced by canopy. Inspired by the wide success of the MF in signal filtering and image denoising [31], [32], [33], the MF is considered to be able to find the ground surface using the signal photons in our case. Moreover, considering the large coverage of canopy when dealing with forest areas, using MF in an iterative way is necessary to find a reliable and accurate ground surface [13]. However, when calculating the median value in MF, it treats all signal photons equally weighted within the filter window. We argue that this treatment ignores the fact that the density of ground photons and canopy photons has very different distributions in the vertical and horizontal directions, which is considered in our definition of the gravity-based density (2). Such facts should be used to estimate the likelihood of a signal photon being a ground photon and shall be considered during the ground photon detection process. Therefore, the anisotropic index (4) is created based on the direction of density to describe the density distribution of signal photons and used as a weight for the iterative median filtering approach [32], [34], [35]. This idea leads to our WIMF algorithm to estimate the best ground surface.

For a signal photon p_i, consider a kernel of size k with weights $W = [w_{i-(k-1/2)}, \ldots, w_{i-1}, w_i, w_{i+1}, \ldots, w_{i+(k+1/2)}]$, the weighted median height of p_i is the value m_i minimizing the following expression:

$$\mathrm{argmin}_{m_i} \sum_{j=1}^{k} w_j \cdot |h_j - m_i| \tag{10}$$

where h_j represents the heights of signal photons inside the kernel. The anisotropic index w_j is calculated for each signal photon based on (4). It is used as a weighting factor in the WIMF process. When canopy exists, a smoothed surface will lie between the canopy top and the ground surface, and it will be much closer to the ground than to the canopy top. This phenomenon is naturally applied to iteratively label photons above the smoothed surface as canopy photons. This weighted median filtering process is repeated to eliminate canopy photons that fall above the estimated ground surface and the noise photons that fall below the estimated ground surface. The iteration stops when the difference between the estimated surface from the current iteration (t) and the estimated surface from the previous iteration $(t-1)$ meets the following condition:

$$\left(\sum_{i=1}^{n} |h_t(i) - h_{t-1}(i)| \right) / n \leq \Delta h \tag{11}$$

in which Δh is the termination threshold used to stop the WIMF process. The final estimated ground surface is regarded as the actual ground surface; signal photons whose elevation is close to the final ground surface will be labeled as ground photon, as shown in Fig. 3(d). An example of the WIMF procedure and the intermediate results is shown in Fig. 3(e).

III. Study Areas and Data

Two full counties in U.S. in Fig. 6 are chosen for evaluation. This is the same study area as our previous work [36]. Tippecanoe is in the west central portion of Indiana State and is regarded as a representative of the plain region for our study since its slope is less than 2° and maximum elevation difference is about 110 m. According to the 2020 census, the county population is 172 780 and has a total area of 1303.4 square km, of which 1294.5 square km or 99.32% is land and 8.9 square km or 0.68% is water. Different from Tippecanoe, Mendocino is located on the northern coast of the California. It is mostly mountains with a slope larger than 6° and elevation difference of 2100 m. It is regarded as a representative of mountain and forest region for this study. As of the 2020 census, the county population is 87 841 and has a total area of 10 040 square km, of which 9080 square km or 90.41% is land and 960 square km or 9.59% is water. Additional information about these two counties can be found in our previous study [36].

The ATL03 data as well as the corresponding ATL08 products are used in this study. The ATL03 level 2 product (version 5) used in this study provides the geolocated photons and can be downloaded at (https://search.earthdata.nasa.gov/search) (accessed on December 20, 2021). For every photon detected by ATLAS, the ATL03 product includes the longitude, latitude, and the height relative to the WGS84 ellipsoid. For convenience of comparison, we transformed the ellipsoid height to the orthometric height with

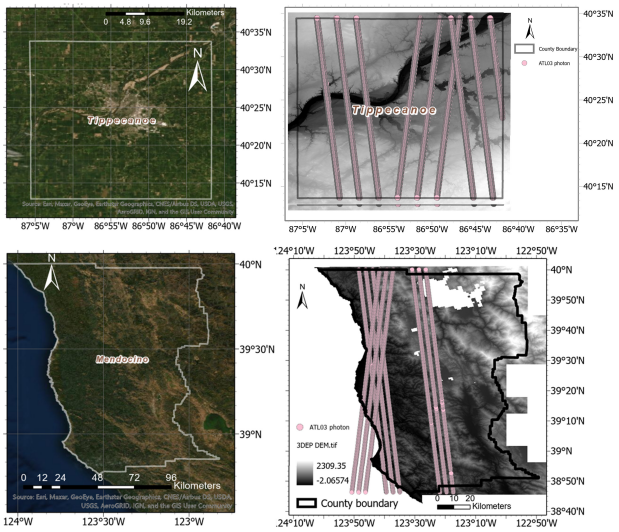

Fig. 6. Satellite image (left), and 3DEP DEM and trajectory of ICESat-2 (right) of the study areas.

respect to the North American Vertical Datum 1988 (NAVD88) using the VDATUM tool [37]. Besides the recorded photons, the ATL03 product also provides the signal finding results from NASA. The signal photons in the ATL03 product include a confidence level ranging from 0 to 4, where 0 represents noise and 4 means high-confidence signal photons. In this study, only ATL03 high-confidence signal photons are considered unless otherwise specified. Based on the ATL03 data, the ATL08 level 3 product (version 5) creates its own signal finding results [13] as well as ground photon finding results for every photon detected by ATLAS, before it segments all terrain information at a fixed step size of 100 m to the benefit of the data users. In this study, the ATL08 data products are downloaded from https://search.earthdata.nasa.gov/search (accessed on December 20, 2021), and their signal finding results and ground finding results for all geolocated photons are used.

The USGS 3-D Elevation Program (3DEP) elevation datasets will be used as the reference data. Fig. 6 shows the USGS 3DEP DEM for the two counties. 3DEP DEMs are produced from airborne lidar under the USGS National Geospatial Program. As shown in Fig. 6, the most recent (released in January 2020) Tippecanoe 3DEP DEM is at a resolution of 2.5-foot (0.76 m) under the Universal Transverse Mercator (UTM) projection. Its horizontal datum is the North American Datum 1983 (NAD83) and the vertical datum is NAVD88. For Mendocino, its 3DEP DEM is at 1-m resolution under the UTM projection and released during 2017–2018. Its horizontal datum is the NAD83 and the vertical datum is the NAVD88. According to the specification of the 3DEP provided by USGS, its vertical accuracy is 10 cm (1σ) in the nonvegetated areas and 15 cm (1σ) in the vegetated areas [38]. Independent quality evaluation for the 3DEP DEMs based on field surveying reveals [36] an elevation uncertainty of 0.039 ± 0.377 and 0.435 ± 1.774 m, respectively, for Tippecanoe and Mendocino.

Experiments are conducted using the geolocated photons of ATL03 data for the two counties. For each county, three tracks are selected, and $3 \times 3 \times 2$ beams (i.e., three tracks, each with three strong–weak beam pairs) are filtered. The computer conducting the experiments has an Intel Core i7-8700 processor with 16-GB RAM. For Tippecanoe where the average length of the tracks is ∼40 km, the wall time of computation is about 3 min per beam. For Mendocino where the average length of the tracks is ∼100 km, the average wall time of computation is about 6 min per beam. We also evaluate the results of signal photon finding and ground photons finding separately. The results of signal photons finding algorithm are to be compared with two other signal photons labeling results from NASA: 1) high-confidence signal photons in the ATL03 product and 2) signal photons in the ATL08 product. The performance of ground photons finding algorithm is evaluated by using the 3DEP DEM as reference to, respectively, compare the ground photons detected by our algorithm and the ground photons labeled in the ATL08 product.

IV. Results of Signal Photon Detection

Fig. 7(a) presents an example of the signal photons labeling results using the gt1l and gt1r beam of track No. 1361, which passes through Tippecanoe. In this case, the gt1l is the weak beam and the gt1r is the strong beam. The solar background noise stands out since the data were collected during the daytime. There are 101 830 and 195 674 received photons in total for the weak beam (gt1l) and strong beam (gt1r), respectively. For both weak beam and strong beam, the ATL08 product gives the least signal photons, whereas our signal photons labeling algorithm offer the most signal photons, especially for the weak beam. The increase rate is, respectively, 104% compared to ATL03 and 15% compared to ATL08 for weak beams and 15% compared to ATL03 and 10% with respect to ATL08 for strong beams. Even when the medium confidence signal photons in ATL03 (shown as yellow dots in Fig. 7) are taken into account, the total numbers of detected signal photons (28 434 for weak beam and 119 284 for strong beam) of ATL03 are still much less than our results (37 473 for weak beam and 132 173 for strong beam). As shown in Fig. 7(a) where the detailed region of each beam is shown, the ATL03 algorithm and ATL08 algorithm tend to miss signal photons at places where terrain becomes inconsistent. In contrast, our algorithm is more robust to uneven topography, mostly due to the introduction of directional region growing based on the novel density definition and the joint utility of weak–strong beam pairs when labeling the signal photons.

Comparing to our signal photon finding algorithm, there are scenarios that ATL03 gives the most signal photons. Shown in Fig. 7(b) is another example of track No. 919 of the same area as Fig. 7(a). However, the data were collected during nighttime. Although the majority of noise is spared due to the absence of the sunlight, the challenge due to the after-pulsing effect still remains. Efforts have been made in the production of both ATL03 and ATL08 to address the impact of the after-pulsing. ATL03 product gives a confidence level flag for each identified signal photon [12], while ATL08 labels each signal photon by combining the results from the DRAGANN algorithm and the confidence level flag

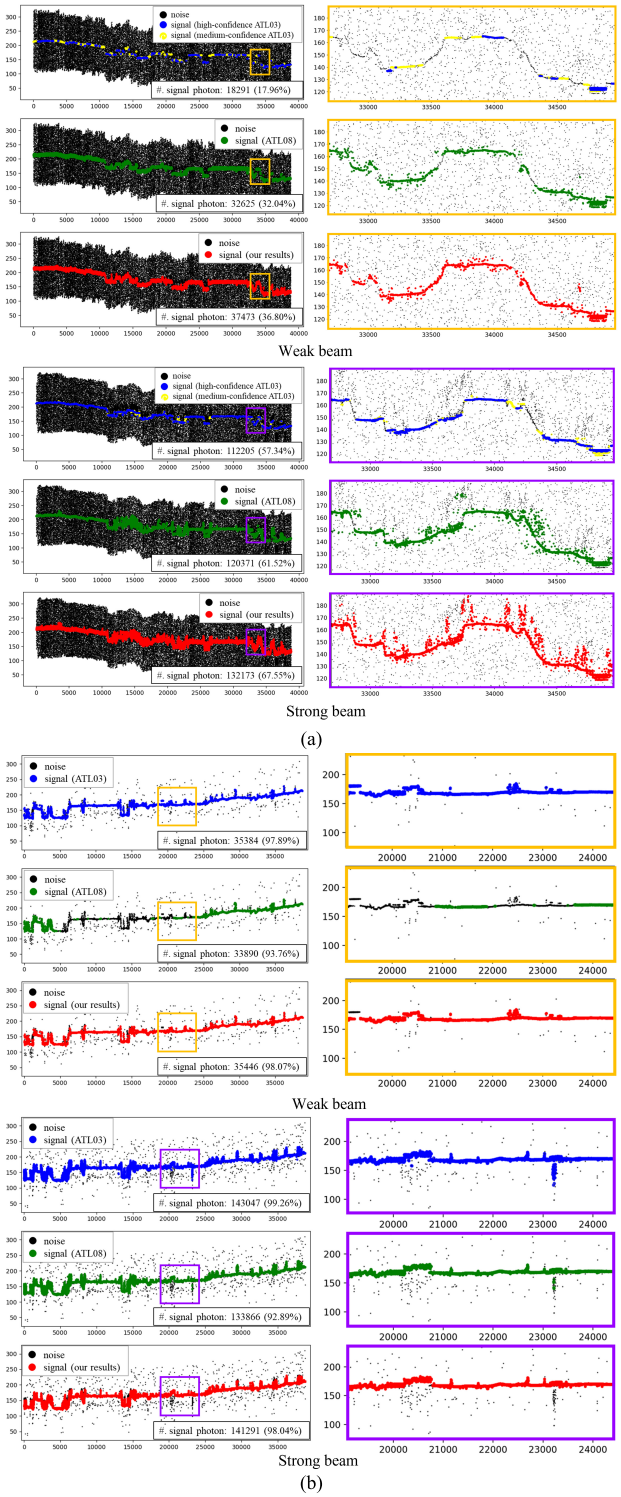

Fig. 7. Comparison of signal photon labeling results in Tippecanoe between ATL03 and ATL08 products, and our results for two tracks collected at (a) daytime and (b) nighttime. The x-axis is the distance along the track (m), and y-axis is the height (m). The purple squared places in (b) are the detailed examination of the after-pulsing effects standing out in strong beams. (a) Track No. 1361 daytime collection. A track of ∼40 km and a subset of 2 km for weak beam (top) and strong beam (bottom). (b) Track No. 919 nighttime collection. A track of ∼40 km and a subset of 5 km for weak beam (top) and strong beam (bottom).

from ATL03 [14]. As shown in the purple squared areas in Fig. 7(b) (right panel), after a strong signal return from the ground surface, the after-pulsing effect stands out. The number of photons in the clusters of the after-pulsing effect shown in Fig. 7(b) (right panel) is around 2000. A closer examination shows that both ATL03 and ATL08 algorithms wrongly labeled them as signal photons, yielding a total of 143 047 signal photons, whereas our algorithm can successfully label these after-pulsing photons as noise, leading to a total of 141 291 signal photons. Although the percentage of after-pulsing photons is only ∼1.4%, their mislabeling as signal photons will considerably affect the shape of the local terrain. This example demonstrates that our method can reduce the chance of mislabeling noise photons to signals when the after-pulsing effect occurs. This robustness is mostly due to the joint use of weak–strong beam pair when calculating the density of a recorded photon.

For Mendocino with uneven topography, two examples of the same track No. 67 collected at daytime and nighttime are shown in Fig. 8. Fig. 8(a) demonstrates the results of beam gt1l (weak) and gt1r (strong) of track No. 67 during the day. As shown in the detail zoomed-in figures [see Fig. 8(a) right], due to the low SNR caused by sunlight, both ATL03 and ATL08 algorithms do not always perform well on the terrain inconsistency when labeling the signal photons, whereas our algorithm is more robust. Even when the medium confidence signal photons [yellow dots in Fig. 8(a)] in ATL03 are taken into account, the total numbers of detected signal photons (97 for weak beam and 9791 for strong beam) are still much less than our results (14 297 for weak beam and 46 396 for strong beam). This is also demonstrated in Fig. 8(b) that gives an example of the results of nighttime collection data of track No. 67. Although the ATL03 algorithm beats the ATL08 signal labeling algorithm in this case, it tends to mislabel the noise photons as signal photons, leading to more wrongly identified signal photons.

From the previous research, it is known that the quality of signal photon finding result is majorly related to the SNR, which in turn is related to the sunlight, terrain slope, and beam type [18]. The overall statistics for the signal photon labeling results are listed in Table I. It can be noticed from the table that the quality of signal photons from ATL03 during nighttime is comparable with ATL08 and our method. Their difference is less than 10% for almost all scenarios. This observation applies to both weak beams and strong beams. However, the statistics for daytime show a noticeable difference. During the daytime, the percentage of the signal photons for ATL03 product ranges from 0.15% to 59.28% of the total number of photons, while for ATL08 product, it ranges from 12.23% to 63.25%. In contrast, our approach achieves 13.04%∼68.52%. The least signal finding results come from the weak beam in Mendocino for the three algorithms (ATL03: 0.15%; ATL08: 12.23%; and ours: 13.04%). We therefore caution users that ATL03 signal photons over forest during daytime may miss significant percentage of true signals. Using signal photons of lower confidence (e.g., medium confidence or low confidence) for such situations may be a realistic practice with care. In the meantime, there is a need to improve signal photon finding method for daytime collections, especially over mountain areas. ALT03 signal points detected during daytime are over

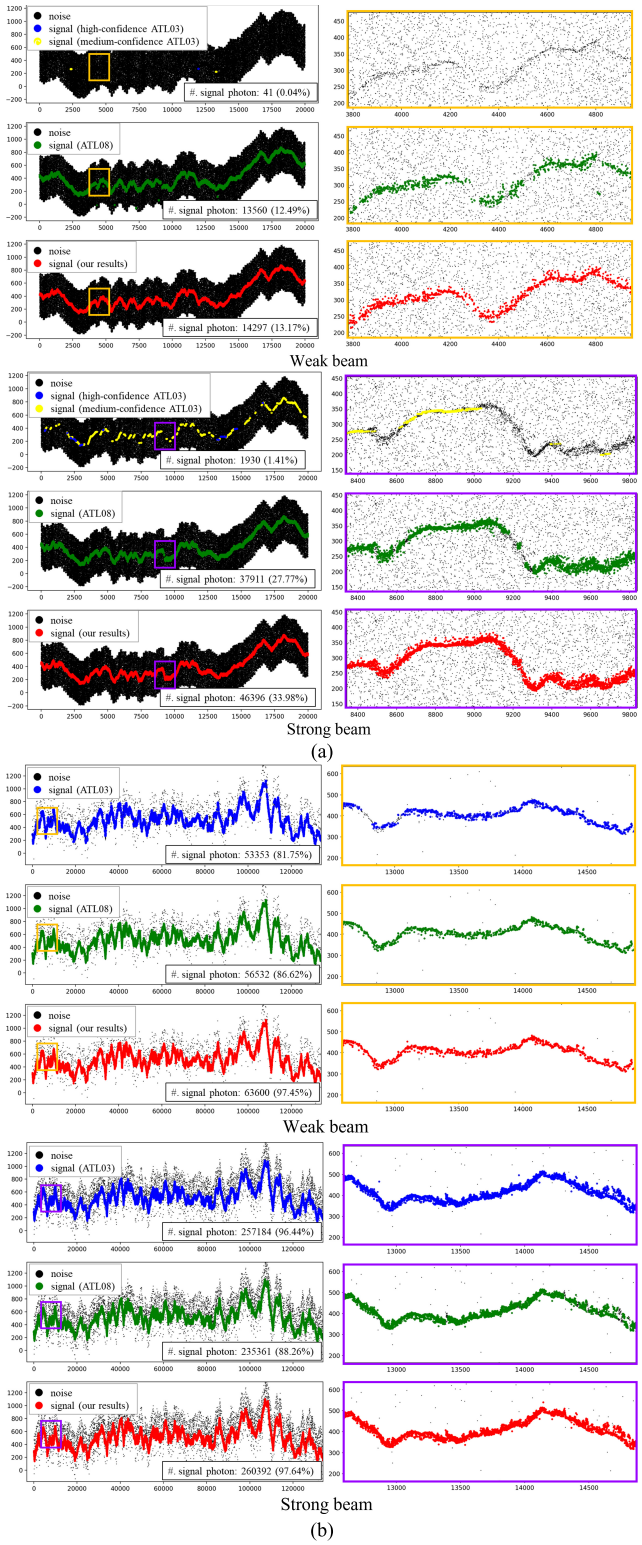

Fig. 8. Comparison of signal photons labeling results in Mendocino between ATL03 and ATL08 products, and our results for two tracks collected at (a) daytime and (b) nighttime. The x-axis is the distance along the track (m), and y-axis is the height (m). (a) Track No. 67 daytime collection. A track of ~20 km and a subset of 3 km for weak beam (top) and strong beam (bottom). (b) Track No. 67 nighttime collection. A track of ~120 km and a subset of 2 km for weak beam (top) and strong beam (bottom).

conservative. Only a fraction of signal photons is recognized under this situation. Compared to the ATL03 product, we can

TABLE I

OVERALL STATISTICS OF SIGNAL PHOTON DETECTION RESULTS (* SIGNAL PHOTONS OF ATL03 ONLY INCLUDE HIGH CONFIDENCE ONES; # FOR COUNT; % FOR PERCENTAGE; THE LEAST PERCENTAGE OF SIGNAL PHOTONS FOR WEAK BEAM (BOLD) AND STRONG BEAM (UNDERLINED)

				Tippecanoe County			Mendocino County		
				ATL03*	ATL08	Ours	ATL03*	ATL08	Ours
Day	Weak Beam	Signal	#	68427	126043	141607	510	42581	45415
			%	18.17	33.46	37.60	**0.15**	12.23	13.04
		Total		376643	376643	376643	348291	348291	348291
	Strong Beam	Signal	#	415113	442846	479750	10471	120858	142068
			%	59.28	63.25	68.52	<u>2.44</u>	28.14	33.08
		Total		700205	700205	700205	429485	429485	429485
Night	Weak Beam	Signal	#	161902	157541	162305	344347	316444	341390
			%	87.69	85.33	87.91	86.84	79.80	86.10
		Total		184631	184631	184631	396525	396525	396525
	Strong Beam	Signal	#	526935	511435	528795	1464991	1234209	1394403
			%	95.33	92.53	95.67	96.92	81.65	92.25
		Total		552744	552744	552744	1511552	1511552	1511552

TABLE II

OVERALL STATISTICS OF THE GROUND PHOTON DETECTION RESULTS (# FOR COUNT; % FOR PERCENTAGE)

				Tippecanoe County		Mendocino County	
				ATL08	Ours	ATL08	Ours
Day	Weak Beam	Ground	#	108226	117507	5319	14415
			%	28.73	31.20	1.53	4.14
		Total		376643	376643	348291	348291
	Strong Beam	Ground	#	414198	419750	7485	20068
			%	59.15	59.95	1.74	4.67
		Total		700205	700205	429485	429485
Night	Weak Beam	Ground	#	135843	138305	74687	101390
			%	73.58	74.91	18.84	25.57
		Total		184631	184631	396525	396525
	Strong Beam	Ground	#	467339	468795	326500	402403
			%	84.55	84.81	21.60	26.62
		Total		552744	552744	1511552	1511552
Total		Ground	#	1125606	1144357	413991	538276
			%	62.04	63.08	15.41	20.04
		Total		1814223	1814223	2685853	2685853

produce up to ten times more signal photons (2.44% versus 33.08% for strong beam in Mendocino), and up to several percentage more signal photons compared to ATL08 product (28.14% versus 33.08% for strong beam in Mendocino). The benefit from our signal photon finding algorithm is more apparent over mountain areas for strong beam data collected during the daytime with respect to ATL03 product. It is less

vulnerable with respect to the reduced SNR, e.g., caused by beam type, sunlight, and terrain slope.

One noticeable feature that can be found for ATL03 product is that the number (or the percentage) of signal photons in each confidence level fluctuates largely under different cases. There are research indicating that the aggregation of signal photons from all of the low, medium, and high confidence levels could capture the majority of the ATLAS pulse shape [12], [39], [40]. Since we only included the high and medium confidence level signal photons in the above analysis, we will further analyze the performance of ATL03 signal photons by adding the low confidence level signal photons in the comparison. For Tippecanoe, the average of the low confidence level signal photons is 13% for daytime data and 3% for nighttime data; for Mendocino, the average is, respectively, 19% and 5% for daytime and nighttime data. This fact clearly indicates that the ATL03 filtering outcomes for nighttime and open areas are more reliable than those for daytime and forest areas [36]. For nighttime collection, the number of high confidence and medium confidence signal photons (over 95%) is sufficient and reliable, while for daytime collection, it is necessary to consider the low confidence signal photons as well; otherwise, up to 19% of ALT03 photons might be missed, possibly causing insufficient number of signal photons to capture the terrain information. Moreover, for strong beam daytime data, including the low confidence data is less risky than do so for weak beam daytime data. To support this observation, Fig. 9(a) illustrates the same track shown in Fig. 7(b). The contribution of the signal photons of the low confidence level is marginal (∼1%) for nighttime data. Similarly, Fig. 9(b) shows the ATL03 signal photons for the same track shown in Fig. 8(a). When the low confidence signal photons are taken into account, the number of signal photons increases from 0.04% to 12.63% for weak beams and from 1.41% to 29.53% for strong beams. Although more signal photons are included, the quality of the detected signal photons is compromised for weak beam, as shown in the orange region Fig. 9(b).

In summary, the performance of the signal detection algorithms is affected largely by SNR. ATL03 algorithm is more likely to mislabel the noise photons as signal photons, even when medium confidence photons are not taken into account. Including the low and medium confidence signal photon requires more caution for different interest areas since their reliability and contribution vary in terms of collection time, surface reflectance, and the beam type. For the ATL08 signal photon labeling algorithm, the major issue is that gaps are more likely to occur at the areas with inconsistent terrain. In particular, the performances of both ATL03 and ATL08 algorithms for signal detection are considerably affected by the after-pulsing effect, which causes mislabeling the noise photons as signal photons. In contrast, with the gravity-based density and the joint utility of the weak–strong beam pair, our algorithm is more robust to SNR and remedies the impact of after-pulsing effect. This is mostly benefited from the directional region growing when dealing with the inconsistent terrain, which largely reduces the probability of omission of signal photons. As such, our signal photon finding algorithm is able to include more signal photons, especially for strong

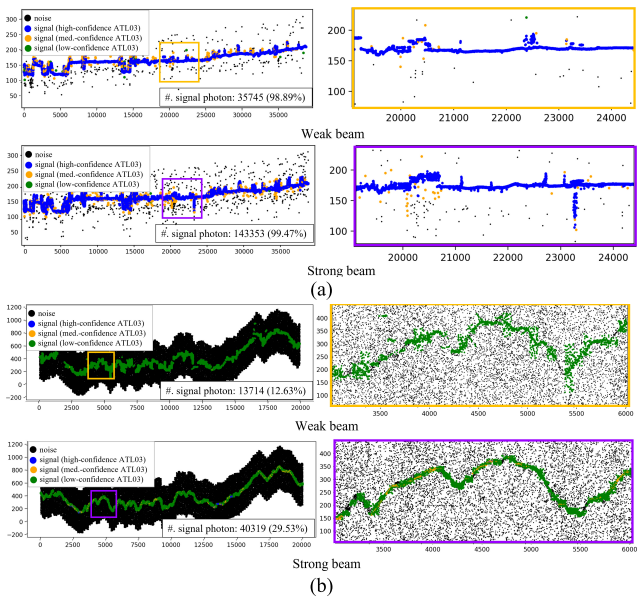

Fig. 9. Low, medium, and high confidence signal photons of ATL03 products for two tracks collected at (a) nighttime in Tippecanoe and (b) daytime in Mendocino. The x-axis is the distance along the track (m), and y-axis is the height (m). (a) Track No. 919 nighttime collection. A track of ∼40 km and a subset of 5 km for weak beam (top) and strong beam (bottom). (b) Track No. 67 daytime collection. A track of ∼20 km and a subset of 3 km for weak beam (top) and strong beam (bottom).

beams collected during daytime over mountain areas, like Mendocino (2.44% versus 33.08%, underlined in Table I). Even for the worst cases which have the lowest SNR (weak beam data collected during daytime in mountain area), our algorithm can still identify more signal photons (0.15% versus 13.04%, bolded in Table I).

V. Results of Ground Photon Detection

As pointed earlier, ground photons are a subset of signal photons. Ground photons are part of the ATL08 products, which are derived independently with the help of the signal photons in ATL03 data [13]. Table II presents the ground photon statistics from ATL08 and our method.

Under all circumstances, we are able to detect more ground photons than the ATL08 product. The gain is rather stable: in average a few percentage (up to 6%), more signal photons are identified as ground photons. For data collected in daytime, this benefit would even triple the number of ground photons detected in ATL08 products over forest areas. The large number of ground photons detected is due to less omission of the signal photon during the signal photon finding procedure, especially for daytime data where a great number of ground photons under canopy may be missed by other algorithms. By including more true signal photons and using anisotropic index to predefine the probability of a signal photon being a ground photon, a more reliable smooth ground surface is extracted, and more reliable ground photons can be detected. In the following, we will use 3DEP DEM as the reference to evaluate the quality of such derived ground photons.

A. Overall Height Accuracy

By comparing the height of detected ground photons and the elevation extracted from the 3DEP DEM, the height accuracy

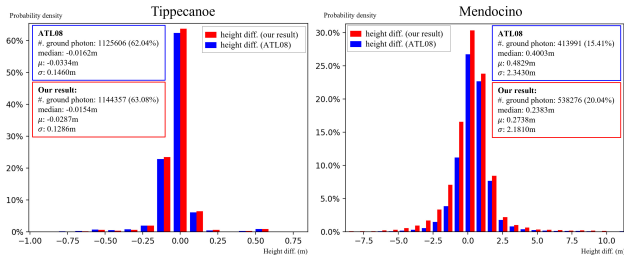

Fig. 10. Histogram of height differences between detected ground photons and 3DEP DEM in Tippecanoe (left) and Mendocino (right).

of ground photon finding results can be analyzed. The overall height differences of ATL08 product and our ground photon finding results are summarized in Fig. 10.

As shown in Fig. 10, for Tippecanoe, our result and ATL08 find similar number of ground photons, 62.04% and 63.08% of the total received photons, respectively. The negative median and mean of the height difference with respect to the 3DEP DEM indicate that the detected ground surfaces from both algorithms are below the reference DEM. Comparing to ATL08, the ground surface from our algorithm is slightly closer to the DEM (mean of height difference: −0.029 versus −0.033 m), and the standard deviation of height difference for our result is slightly better (0.129 versus 0.146 m). It is noticed that for an area with not much canopy coverage and smooth topography, the detected ground surfaces from both methods are quite close and reliable with reference to the 3DEP DEM.

For Mendocino, the advantage of our algorithm is more obvious, as shown in Fig. 10. On the one hand, it offers up to 5% (124 285) more ground photons (ours: 20.04%; ATL08: 15.41%), while on the other hand, the detected ground surface is also much closer to the reference DEM. For ATL08, its positive mean (0.483 m) of height differences suggests that ATL08 product is higher than the reference DEM, whereas the average ground surface from our algorithm is 0.274 m over the reference DEM. This improvement is mainly due to the anisotropic density concept and the joint utility of the weak–strong beam pairs. The anisotropic index is able to estimate the probability of a signal photon being a ground photon. The impact of canopy photons is lessened. As such, therefore, the ground finding result from our algorithm achieves an average ground surface closer to the reference DEM than the ATL08 product. The standard deviation of the height difference of our result is 16 cm (2.181 versus 2.343 m) smaller than the one of the ATL08 product.

Compared to the height difference for Tippecanoe, the height accuracy of the detected ground photons, either from ATL08 product or our method, is much poorer for Mendocino, and the standard deviation of the height differences is over 2 m. Therefore, one should use the detected ground surface with care when working with an area of interest that has large canopy coverage and low SNR due to large terrain slope.

B. Height Accuracy in Terms of the Beam Type

The energy of the laser beam has a large impact on the number of received signal photons per footprint. The SNR varies largely with respect to the beam type due to the

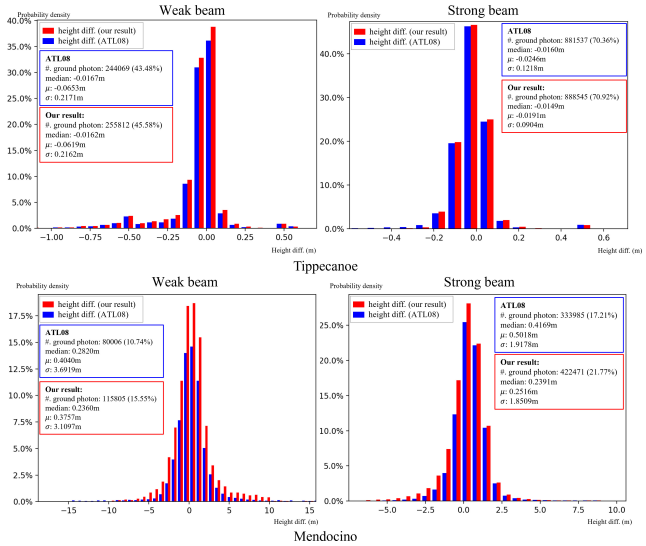

Fig. 11. Histogram of height differences between detected ground photons and 3DEP DEM in terms of weak beam and strong beam for Tippecanoe (top) and Mendocino (bottom).

4:1 energy difference of the strong beam and weak beam. This in turn affects the quality of signal photon finding and ground photon finding results. Fig. 11 summarizes the height difference of ground photons with the reference DEM in terms of the beam type. For our method, the precision (standard deviation of height difference) of the detected ground photons for strong beam is approximately twice better than the weak beam (Tippecanoe: 0.090 m for strong beam and 0.216 m for weak beam; Mendocino: 1.851 m for strong beam and 3.110 m for weak beam). For the mean of height difference of the detected ground photons, the strong beam still holds a better performance (Tippecanoe: −0.019 m for strong beam and −0.062 m for weak beam; Mendocino: 0.252 m for strong beam and 0.376 m for weak beam). Similar relations are also found from the ATL08 products.

Speaking of the number of the detected ground photons, the two algorithms perform rather differently, as shown in Fig. 11. For Tippecanoe, our algorithm detects 2% more ground photons than ATL08 algorithm for weak beam; meanwhile, it only gives 0.6% more ground photons for strong beam. While for Mendocino, as many as 5% more ground photons are found by our algorithm for weak beam and 4% more ground photons are offered for strong beam. For the height accuracy comparison between the two algorithms, our algorithm shows only a slightly better performance in Tippecanoe but demonstrates a great improvement in Mendocino. The improvement is majorly on the mean of the height differences referred to 3DEP DEM for the strong beam (0.252 versus 0.502 m); and for the weak beam, the standard deviation of the height differences is decreased by 0.58 m (from 3.692 to 3.110 m) by our algorithm. For the strong beam data, our algorithm has a smaller chance to miss the ground photons under dense canopy due to the directional region growing, and the anisotropic index assures that these ground photons have a larger weight during the ground finding procedure. Therefore, a more reliable ground surface can be extracted (significant improvement on the average height difference). For the weak beam, the much lower

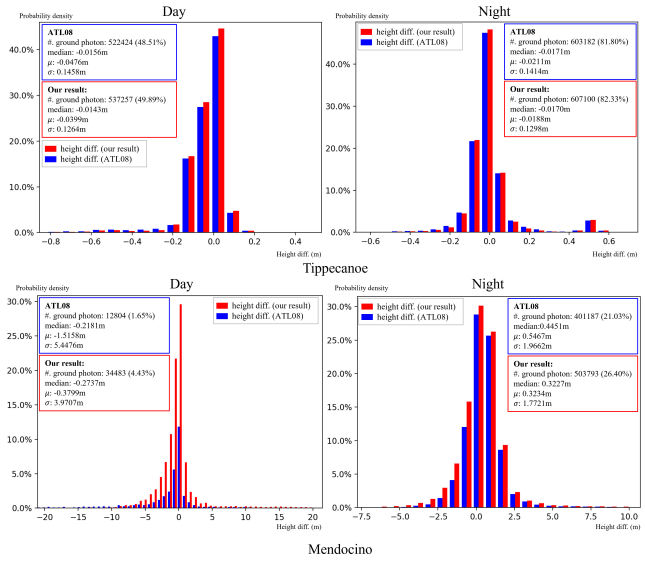

Fig. 12. Histogram of height differences between the detected ground photons and 3DEP DEM in terms of daytime and nighttime for Tippecanoe (top two) and Mendocino (bottom two).

laser energy leads to fewer or even none ground photons under dense canopy. Thus, the improvement on the overestimated ground surface (average height difference) in Mendocino is limited. Moreover, the WIMF algorithm in ground finding procedure can achieve a smoother ground surface and a more significant improvement on the standard deviation of the height difference.

C. Diurnal Variation of Height Accuracy

The SNR varies largely with respect to sunlight, which affects the quality of signal photon finding results and will in turn affect the quality of ground finding results. It is worthwhile to examine the performance of the two algorithms in terms of diurnal acquisition time. To analyze the diurnal variation of height accuracy, the height differences of ground photons with respect to the reference DEM are summarized in Fig. 12. For Tippecanoe, the number of ground photons from nighttime is as twice as the number of ground photons from daytime, whereas for Mendocino, this ratio is changed to as many as six (6). For Mendocino, the uneven topography further decreases the SNR on top of the decrease brought by solar background noise, causing extremely few ground photons (4.43%) detected for daytime data. Although the ground finding results are similar for the two algorithms for Tippecanoe, for Mendocino, the mean of height differences can be improved by 1.14 m (ATL08 algorithm: -1.516 m; our algorithm: -0.380 m), and the standard deviation of height differences can be decreased by 1.48 m (ATL08 algorithm: 5.448 m; our algorithm: 3.971 m). The improvement can be attributed by the weighting capability in WIMF and less omission of the signal photons during the signal photon finding procedure. By including more true signal photons and using anisotropic index to predefine the probability of a signal photon being a ground photon, a more reliable smooth ground surface is extracted.

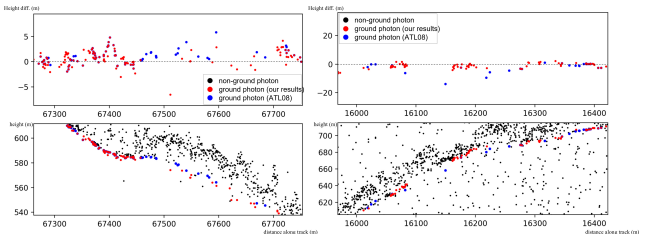

Fig. 13. Example of an overestimated ground under the impact of canopy coverage in nighttime (left) and an underestimated ground under the impact of canopy coverage and solar background noise in daytime (right).

As shown in Fig. 12, the average ground surface in Tippecanoe from daytime data is $\sim$0.2 m lower than the average ground surface from nighttime data (mean of height differences: -0.040 m for day and -0.021 m for night), and in Mendocino, it is $\sim$0.6 m lower (mean of height differences: -0.380 m for day and 0.323 m for night). From the comparison between daytime data and nighttime data in these two counties, it can be concluded that the solar background noise causes a more underestimated ground surface. For the lower right figure in Fig. 12, which shows the results evaluation for nighttime data in Mendocino, the positive mean height difference suggests that the canopy coverage has very different impact than the solar background noise; the former leads to a more overestimated ground surface, while the latter reduces the SNR. Their combined impact leads to a negative mean height difference for the daytime data in Mendocino.

Both a dense canopy coverage and a low SNR caused by solar background could lead to a vague ground surface, which is the source of the height differences between the ground from ICESat-2 and 3DEP DEM, but their impact on the results is quite different. The challenge brought by the dense canopy is that very few ground photons can be detected beneath it. For tracks collected at night as shown in the left of Fig. 13, the ground surface beneath dense canopy is barely noise photon free, and the height of the estimated ground surface would be overestimated since some canopy photons can be included during the ground photon finding. However, much more noise photons during the daytime are introduced, as shown in the right figure of Fig. 13. The disturbance on the true ground surface consists of two aspects: 1) the noise photons below the ground surface raised by the after-pulsing effect caused by detector saturation, ionization effect within the PMTs, and internal optical reflections in the receiver [10] and 2) the canopy photons above the ground surface. In the signal photon finding process, our algorithm is designed to include as many signal photons as possible, which introduces the noise photons very close to the ground photons as signal photons. The following WIMF used to estimate the ground surface is a smooth filtering method, which tends to underestimate the height of the ground surface, increasing the probability of labeling those mislabeled noise photons as ground photons. For the data in Mendocino, despite the fact that the mean of the height difference is improved by $\sim$1.14 m through our algorithm (ATL08 algorithm: -1.516 m; our algorithm: -0.380 m) and the standard deviation of the height difference is decreased from 5.45 to 3.97 m, the final achieved ground

accuracy for Mendocino is poorer than the ground accuracy for Tippecanoe. Therefore, for researchers interested in areas with an uneven topography covered with dense canopy, ground information extracted from ATLAS geolocated photons shall be used with caution. One may expect a large variation on the precision of the ground surface (daytime data: up to 5.45 m; nighttime: up to 1.97 m).

VI. Conclusion

In this study, the gravity-based density method, or GRADWIT, is proposed to cluster the geolocated photons of ICESat-2 ATLAS. Different from the conventional definition of the density which is the number of photons in a fixed area, we define the density of a geolocated photon as a vector based on the gravitational-force model. The magnitude of the density is a relationship of the distance between the target photon and its surrounding photons within each beam; then, the density of photons from both beams is used simultaneously.

To achieve reliable outcome, the signal finding method is formulated as a two-step procedure: key photon selection and signal photon finding. An energy function is built with a data cost term and a smooth cost term. The data cost term is the combination of the density of photons from the weak–strong beam pair, whereas the smooth cost term is the similarity between a photon and its neighbors. Under this formulation, we are able to apply the graph-cut method to determine key photons in a reliable and effective way. To further detect all signal photons, a directional region growing algorithm is applied, in which both of the density threshold and distance threshold are adaptive. Finally, we introduce the anisotropic index as a weighting factor to the existing iterative MF for the subsequent ground photon finding process. The key for ground photon finding is the anisotropic index, which is defined based on the calculated density direction to describe the probability of a signal photon being a ground photon. The WIMF algorithm is then introduced to find the estimated ground surface. The ground photons are labeled by identifying the photons close to the ground surface.

For signal photon detection, the performance of an algorithm varies according to the SNR (caused by beam type, sunlight, and terrain slope variation). Speaking of the number of detected signal photons, the performance of all algorithms (ATL03, ATL08, and ours) is comparable; the differences between them are less than 10% for almost all scenarios in terms of the data collection time, beam type, and surface reflectance. All three algorithms could detect more signal photons for nighttime data than daytime data. The fluctuation of the SNR caused by steep slope is a challenge for both ATL03 and ATL08, where gaps are often found through a detailed examination. This inconsistency happens for both ATL03 and ATL08 regardless the data collection time. When dealing with ATL03 signal photons, including or excluding the low confidence ones needs care. For nighttime data, including low confidence data does not further contribute to the information captured by the high and medium confidence photons. For daytime strong beam data, including the low confidence signal photons would be beneficial without compromising the reliability largely, while for daytime weak beam data, it needs additional validation. Meanwhile, the evaluation shows that our algorithm is more robust to the change of the SNR brought by the data collection time and uneven topography. Another major progress achieved by our algorithm is that the signal photon finding results are free from the impact of the cluster of noise photons caused by the after-pulsing effect. Unlike the ATL03 algorithm and ATL08 algorithm, our signal photon finding algorithm does not mislabel the noise-photon cluster below the ground surface as signal photons. This can be attributed to the combined use of the density of photons from the weak–strong beam pair for key photon selection and the conduction of directional region growing along the estimated slope direction.

For the ground photon detection algorithm, the results are compared with the ATL08 ground photons. It is noticed that the height accuracy of the detected ground photons is affected by canopy coverage and SNR (indirectly). It is shown that a dense canopy coverage would cause a more overestimated ground surface, while the low SNR may lead to a more underestimated ground surface. The benefits brought by the gravity-based density concept and the combined use of weak–strong beam pair of our algorithm are magnified most when handling the data collected during the daytime in Mendocino. The average ground surface defined by the detected ground photons is less underestimated by $\sim$75% and the variance of the height differences is decreased by $\sim$27%. Besides the advantage of our algorithm stands out when processing the strong beam data in Mendocino as well, the average ground surface defined by the detected ground photons is less overestimated by $\sim$50%. In summary, the potential of the ATLAS data for ground surface mapping is furtherer explored based on the results achieved by previous research. Using the geolocated photons from the weak–strong beam pair simultaneously during the signal photon finding process succeeds to get a reliable and precise estimated ground surface.

Future efforts can be made in several fronts. We would suggest to explore the joint use of weak–strong beam pairs in multiple steps of the entire processing pipeline, including the use of local surface fitting for ground detection. There is a need to adopt and modify this work to urban areas, where there are substantial man-made objects, which may need special care in handling large vertical discontinuities. We also expect that the work can be further modified for the production of future versions of ICESat-2 data products, especially, the ATL03 and ATL08 product as well as their derivatives.

References

[1] T. Sun, J. Qi, and H. Huang, "Discovering forest height changes based on spaceborne LiDAR data of ICESat-1 in 2005 and ICESat-2 in 2019: A case study in the Beijing-Tianjin-Hebei region of China," *Forest Ecosyst.*, vol. 7, no. 1, pp. 1–12, Dec. 2020, doi: 10.1186/s40663-020-00265-w.

[2] B. E. Schutz, H. J. Zwally, C. A. Shuman, D. Hancock, and J. P. DiMarzio, "Overview of the ICESat mission," *Geophys. Res. Lett.*, vol. 32, no. 21, 2005, Art. no. L21S01, doi: 10.1029/2005GL024009.

[3] L. Magruder, T. Neumann, and N. Kurtz, "ICESat-2 early mission synopsis and observatory performance," *Earth Space Sci.*, vol. 8, no. 5, May 2021, Art. no. e2020EA001555, doi: 10.1029/2020EA001555.

[4] T. A. Neumann et al., "The ice, cloud, and land elevation satellite—2 mission: A global geolocated photon product derived from the advanced topographic laser altimeter system," *Remote Sens. Environ.*, vol. 233, Nov. 2019, Art. no. 111325, doi: 10.1016/j.rse.2019.111325.

[5] Y. Ma et al., "Photon-counting LiDAR: An adaptive signal detection method for different land cover types in coastal areas," *Remote Sens.*, vol. 11, no. 4, p. 471, Feb. 2019, doi: 10.3390/rs11040471.

[6] T. Markus et al., "The ice, cloud, and land elevation satellite-2 (ICESat-2): Science requirements, concept, and implementation," *Remote Sens. Environ.*, vol. 190, pp. 260–273, Mar. 2017, doi: 10.1016/j.rse.2016.12.029.

[7] A. L. Neuenschwander and L. A. Magruder, "Canopy and terrain height retrievals with ICESat-2: A first look," *Remote Sens.*, vol. 11, no. 14, p. 1721, Jul. 2019, doi: 10.3390/rs11141721.

[8] A. J. Martino, T. A. Neumann, N. T. Kurtz, and D. McLennan, "ICESat-2 mission overview and early performance," *Proc. SPIE*, vol. 11151, p. 11, Oct. 2019, doi: 10.1117/12.2534938.

[9] L. A. Magruder, M. E. Wharton III, K. D. Stout, and A. L. Neuenschwander, "Noise filtering techniques for photon-counting ladar data," *Proc. SPIE*, vol. 8379, May 2012, Art. no. 83790Q, doi: 10.1117/12.919139.

[10] X. Lu et al., "Enabling value added scientific applications of ICESat-2 data with effective removal of afterpulses," *Earth Space Sci.*, vol. 8, no. 6, Jun. 2021, Art. no. e2021EA001729, doi: 10.1029/2021EA001729.

[11] S. Palm, Y. Yang, U. Herzfeld, and D. Hancock, "ICESat-2 algorithm theoretical basis document for the atmosphere. Part I: Level 2 and 3 data products," NASA, Washington, DC, USA, Tech. Rep., 2021.

[12] T. Neumann et al., "Algorithm theoretical basis document (ATBD) for global geolocated photons ATL03," NASA, Washington, DC, USA, Tech. Rep., 2020.

[13] A. Neuenschwander and K. Pitts, "The ATL08 land and vegetation product for the ICESat-2 mission," *Remote Sens. Environ.*, vol. 221, pp. 247–259, Feb. 2019, doi: 10.1016/j.rse.2018.11.005.

[14] A. Neuenschwander and K. Pitts. (2020). *Algorithm Theoretical Basis Document (ATBD) for Land-Vegetation Along-Track Products (ATL08)*. Accessed: Jun. 21, 2022. [Online]. Available: https://nsidc.org/sites/nsidc.org/files/technical-references/ICESat2_ATL08_ATBD_r003.pdf

[15] J. Zhang and J. Kerekes, "An Adaptive density-based model for extracting surface returns from photon-counting laser altimeter data," *IEEE Geosci. Remote Sens. Lett.*, vol. 12, no. 4, pp. 726–730, Apr. 2015, doi: 10.1109/LGRS.2014.2360367.

[16] S. Nie et al., "Estimating the vegetation canopy height using micro-pulse photon-counting LiDAR data," *Opt. Exp.*, vol. 26, no. 10, pp. A520–A540, May 2018, doi: 10.1364/oe.26.00a520.

[17] X. Zhu et al., "A noise removal algorithm based on OPTICS for photon-counting LiDAR data," *IEEE Geosci. Remote Sens. Lett.*, vol. 18, no. 8, pp. 1471–1475, Aug. 2021, doi: 10.1109/LGRS.2020.3003191.

[18] Z. Zhang, X. Liu, Y. Ma, N. Xu, W. Zhang, and S. Li, "Signal photon extraction method for weak beam data of ICESat-2 using information provided by strong beam data in mountainous areas," *Remote Sens.*, vol. 13, no. 5, pp. 1–29, Mar. 2021, doi: 10.3390/rs13050863.

[19] M. Ester, H.-P. Kriegel, J. Sander, and X. Xu. (1996). *A Density-Based Algorithm for Discovering Clusters in Large Spatial Databases With Noise*. [Online]. Available: http://www.aaai.org

[20] W. E. Wright, "Gravitational clustering," *Pattern Recognit.*, vol. 9, no. 3, pp. 151–166, 1977.

[21] Z. Wang et al., "Clustering by local gravitation," *IEEE Trans. Cybern.*, vol. 48, no. 5, pp. 1383–1396, May 2018, doi: 10.1109/TCYB.2017.2695218.

[22] P. Zhang and K. She, "A novel hierarchical clustering approach based on universal gravitation," *Math. Problems Eng.*, vol. 2020, pp. 1–15, Feb. 2020, doi: 10.1155/2020/6748056.

[23] P. A. Tipler, *Physics*. New York, NY, USA: Worth Publishers, 1976.

[24] H. Abdi and L. J. Williams, "Principal component analysis," *Wiley Interdiscipl. Rev., Comput. Statist.*, vol. 2, no. 4, pp. 433–459, Jul. 2010, doi: 10.1002/wics.101.

[25] Y. Boykov and V. Kolmogorov, "An experimental comparison of min-cut/max-flow algorithms for energy minimization in vision," *IEEE Trans. Pattern Anal. Mach. Intell.*, vol. 26, no. 9, pp. 1124–1137, Sep. 2004, doi: 10.1109/TPAMI.2004.60.

[26] Y. Boykov, O. Veksler, and R. Zabih, "Fast approximate energy minimization via graph cuts," *IEEE Trans. Pattern Anal. Mach. Intell.*, vol. 23, no. 11, pp. 1222–1239, Nov. 2001, doi: 10.1109/34.969114.

[27] S. Ural and J. Shan, "Min-cut based semantic building labeling for airborne LiDAR data," *ISPRS Ann. Photogramm., Remote Sens. Spatial Inf. Sci.*, vol. 5, no. 2, pp. 305–312, Aug. 2020, doi: 10.5194/isprs-annals-V-2-2020-305-2020.

[28] J. Gu and R. G. Congalton, "Individual tree crown delineation from UAS imagery based on region growing by over-segments with a competitive mechanism," *IEEE Trans. Geosci. Remote Sens.*, vol. 60, pp. 1–11, 2022, doi: 10.1109/TGRS.2021.3074289.

[29] Y. Ma, J. Anderson, S. Crouch, and J. Shan, "Moving object detection and tracking with Doppler LiDAR," *Remote Sens.*, vol. 11, no. 10, p. 1154, May 2019, doi: 10.3390/rs11101154.

[30] Y. Wei, S. Su, J. Lu, and J. Zhou, "FGR: Frustum-aware geometric reasoning for weakly supervised 3D vehicle detection," in *Proc. IEEE Int. Conf. Robot. Autom. (ICRA)*, May 2021, pp. 4348–4354, doi: 10.1109/ICRA48506.2021.9561245.

[31] U. Erkan, L. Gökrem, and S. Enginoğlu, "Different applied median filter in salt and pepper noise," *Comput. Electr. Eng.*, vol. 70, pp. 789–798, Aug. 2018, doi: 10.1016/j.compeleceng.2018.01.019.

[32] G. George, R. M. Oommen, S. Shelly, S. S. Philipose, and A. M. Varghese, "A survey on various median filtering techniques for removal of impulse noise from digital image," in *Proc. Conf. Emerg. Devices Smart Syst. (ICEDSS)*, Mar. 2018, pp. 235–238, doi: 10.1109/ICEDSS.2018.8544273.

[33] A. Shah et al., "Comparative analysis of median filter and its variants for removal of impulse noise from gray scale images," *J. King Saud Univ., Comput. Inf. Sci.*, vol. 34, no. 3, pp. 505–519, Mar. 2022, doi: 10.1016/j.jksuci.2020.03.007.

[34] D. Brownrigg, "The weighted median filter," *Commun. ACM*, vol. 27, no. 8, pp. 807–818, Aug. 1984, doi: 10.1145/358198.358222.

[35] T. Chen and H. R. Wu, "Adaptive impulse detection using center-weighted median filters," *IEEE Signal Process. Lett.*, vol. 8, no. 1, pp. 1–3, Jan. 2001, doi: 10.1109/97.889633.

[36] X. Tian and J. Shan, "Comprehensive evaluation of the ICESat-2 ATL08 terrain product," *IEEE Trans. Geosci. Remote Sens.*, vol. 59, no. 10, pp. 8195–8209, Oct. 2021, doi: 10.1109/TGRS.2021.3051086.

[37] K. M. Hess, "VDATUM manual for development and support of NOAA's vertical datum transformation tool, VDATUM," Office Coast Surv., Nat. Geodetic Surv., NOAA, Washington, DC, USA, Tech. Rep., 2012.

[38] S. T. Arundel et al., "Preparing *The National Map* for the 3D elevation program—Products, process and research," *Cartogr. Geograph. Inf. Sci.*, vol. 42, pp. 40–53, Aug. 2015, doi: 10.1080/15230406.2015.1057229.

[39] K. M. Brunt, T. A. Neumann, and B. E. Smith, "Assessment of ICESat-2 ice sheet surface heights, based on comparisons over the interior of the Antarctic ice sheet," *Geophys. Res. Lett.*, vol. 46, no. 22, pp. 13072–13078, Nov. 2019, doi: 10.1029/2019GL084886.

[40] B. Smith et al., "Land ice height-retrieval algorithm for NASA's ICESat-2 photon-counting laser altimeter," *Remote Sens. Environ.*, vol. 233, Nov. 2019, Art. no. 111352, doi: 10.1016/j.rse.2019.111352.

Xiangxi Tian received the M.S. degree in geomatics engineering from Purdue University, West Lafayette, IN, USA, in 2019, where she is currently pursuing the Ph.D. degree with the School of Civil Engineering.

Her research interests include aerospace lidar, photogrammetry, image-based navigation, machine learning, and digital elevation models.

Jie Shan (Senior Member, IEEE) received the Ph.D. degree in photogrammetry and remote sensing from Wuhan University, Wuhan, China, in 1989.

He has worked at Universities in China, Germany, and Sweden. He is currently a Professor with the School of Civil Engineering, and Department of Earth, Atmospheric and Planetary Sciences, Purdue University, West Lafayette, IN, USA. His research interests include sensor geometry and positioning, object extraction and reconstruction from images and point clouds, urban remote sensing, pattern recognition, and geospatial data mining.

Prof. Shan is a recipient of multiple best paper awards and elected as an ASPRS Fellow. He serves on the editorial boards of several remote sensing journals.